https://doi.org/10.5194/essd-2025-234
Preprint. Discussion started: 17 June 2025

A global dataset of high-resolution CO_2 enhancements derived from OCO-3 measurements

Pingyu Fan[1,6], Jiangong Liu[2], Yuan Xu[3], Bo Huang[4], Chris Webster[5], and Yulun Zhou[1,6,7]

[1]Department of Urban Planning and Design, The University of Hong Kong, Hong Kong, China
[2]Department of Earth and Environmental Engineering, Columbia University, New York, United States
[3]Department of Geography and Resources Management, The Chinese University of Hong Kong, Hong Kong, China
[4]Department of Geography, The University of Hong Kong, Hong Kong, China
[5]Urban Systems Institute, The University of Hong Kong, Hong Kong, China
[6]The University of Hong Kong Shenzhen Institute of Research and Innovation, Shenzhen, China
[7]Musketeers Institute of Data Science, The University of Hong Kong, Hong Kong, China

Correspondence: Yulun Zhou (yulunzhou@hku.hk)

Abstract. We present a novel global dataset of CO_2 enhancements (ΔXCO_2) derived by fusing NASA's OCO-3 satellite and NOAA ground-based observations. CO_2 enhancements quantify the spatially resolved excess in atmospheric CO_2 concentrations arising from anthropogenic emissions, biospheric CO_2 exchanges, and atmospheric CO_2 transport. Leveraging decades of monthly CO_2 measurements from eight remote stations strictly selected from NOAA ESRL network, such as the Mauna Loa station, we address the critical challenge of isolating localized CO_2 signals from background concentrations by developing a latitude-dependent global CO_2 baseline model that effectively captures spatial and seasonal variability in background CO_2. The developed baseline model demonstrates near-perfect hemispheric predictive accuracy (Northern: R^2=0.988, RMSE=1.78 ppm; Southern: R^2=0.995, RMSE=1.09 ppm). Spatially explicit ΔXCO_2 is then estimated by removing the column-corrected background CO_2 from co-located OCO-3 observations. Validations of the estimated ΔXCO_2 against tropospheric NO_2 (R^2=0.896) and prior in-situ urban CO_2 measurements, along with the dataset's high spatiotemporal resolution ($\sim$ 3 km^2), demonstrates its potential for tracking anthropogenic and biospheric CO_2 dynamics. Global ΔXCO_2 maps reveal mean CO_2 enhancements of 0.58 $\pm$ 1.81 ppm, with urban areas exhibiting 1.5-fold higher enhancements (1.43 $\pm$ 2.04 ppm). North Hemisphere land areas exhibits an approximately 81% higher ΔXCO_2 average (0.67 $\pm$ 1.98 ppm) compared to the South Hemisphere (0.37 $\pm$ 1.32 ppm), with urban enhancements amplifying this hemispheric contrast up to 95%. Comprising 54 million observations across more than 200 countries, this open-access dataset provides an alternative metric for monitoring complex atmospheric CO_2 variability and actionable insights for regional climate policies, available at https://doi.org/10.5281/zenodo.15209825.

1 Introduction

Mapping global CO_2 enhancements with fine spatio-temporal resolution is essential for tracking anthropogenic and natural CO_2 sources, validating emission inventories and climate models, and assessing localized climate impacts, including effects on agricultural productivity. The CO_2 enhancement (ΔXCO_2) quantifies the combined influence of anthropogenic carbon emissions, the net CO_2 exchange between vegetation and the atmosphere, and large-scale atmospheric transport processes

https://doi.org/10.5194/essd-2025-234
Preprint. Discussion started: 17 June 2025

(Kiel et al., 2021; Mitchell et al., 2018; Reuter et al., 2019; Lei et al., 2022). A positive ΔXCO_2 signifies the net positive impacts of CO_2 sources and sinks with atmospheric transport processes on accumulation of atmospheric CO_2 concentration (Park et al., 2021; Kiel et al., 2021; Mitchell et al., 2018). ΔXCO_2 can become negative when enhanced terrestrial CO_2 uptake surpassing the amount emitted and atmospheric conditions such as prevailing wind result in a net decline in atmospheric CO_2 compared to long-term baseline. Accurate global ΔXCO_2 measurements are critical for understanding the current net contributions of local human and plant activities on atmospheric CO_2 increases. These fundamental measurements underpin the development of targeted strategies for future emission cuts and climate mitigation. Nevertheless, a comprehensive global dataset of CO_2 enhancements remains absent.

Carbon satellites have been reported as objective, independent data sources for monitoring spatiotemporal disparities of atmospheric CO_2 conditions (Pan et al., 2021; Nisbet and Weiss, 2010; Schwandner et al., 2017), by providing the top-down observations of column-averaged dry-air mole fraction of CO_2 (XCO_2; ppm). Satellite-derived CO_2 observations enhance data disclosure, transparency, and data equity especially in underdeveloped countries where data infrastructure is lacking and the accounting capacity of environmental departments is often weak. Moreover, the global coverage and high spatiotemporal resolution of satellite instruments are key advantages that support the characterization of large-scale fine-grained atmospheric CO_2 levels. These capabilities, first, enable effective comparisons among multiple sites, cities, and countries; second, help refine the general patterns underlying local CO_2 variability, and ultimately, aid CO_2 mitigation efficacy by facilitating local governments making dynamic and targeted decisions.

Mapping ΔXCO_2 based on satellite remote-sensing data remains challenging, although CO_2 satellites have been popular for global atmospheric observations (Streets et al., 2013). The century-long persistence of CO_2 causes the immensely strong signal and notable spatial variability of background CO_2 concentration in the atmosphere, even in desert-like places (Hakkarainen et al., 2019). This accumulation masks the true CO_2 signals from local human and natural processes. Localized atmospheric CO_2 fluctuations are around two orders of magnitude smaller than the background CO_2 concentration (Canadell et al., 2023; Reuter et al., 2019). This substantial difference complicates the global differentiation of enhanced CO_2 signals from the accumulative trend of background CO_2. Therefore, a key step in isolating localized ΔXCO_2 is deducting accurate fine-resolution background CO_2 concentration from the satellite CO_2 observations.

Satellite-driven ΔXCO_2 measurements are typically single site-specific, individual city-specific, or estimated from multiple-site gradients, rather than offering spatially-continuous coverage. Previous efforts to correct background CO_2 concentration have struggled with scale and seasonal sensitivity (Lindenmaier et al., 2014; Verhulst et al., 2017; Zeng et al., 2021; Miller et al., 2020; Che et al., 2024; Kort et al., 2012; Schneising et al., 2013). These issues constrain the effectiveness in delivering large-scale spatial analysis for fine-resolution ΔXCO_2 data. Site-specific ΔXCO_2 estimates are derived from the difference between satellite observation of atmospheric CO_2 and CO_2 records at ground-truth stations with minimal human and plant interference. These ground-truth stations include remote in-site stations from the Total Carbon Column Observing Network (Kiel et al., 2021) and mountaintop CO_2 observation sites in Salt Lake County, North America (Mitchell et al., 2018). City-specific ΔXCO_2 estimates rely on the deviations of satellite observations in urban centers from the daily median (Hakkarainen et al., 2016; Park et al., 2021) or monthly median (Labzovskii et al., 2019) remote-sensing CO_2 observations in rural areas assuming that rural

https://doi.org/10.5194/essd-2025-234
Preprint. Discussion started: 17 June 2025

atmospheric CO_2 concentration should be considerably lower than that in urban cores (Wu et al., 2020; Reuter et al., 2019; Ye et al., 2020). The former site-specific approach cannot be effectively generalized for regional or global applications due to significant spatial heterogeneity in atmospheric conditions. The latter city-specific approach is sensitive to the seasonal timing of satellite overpasses, since seasonal biospheric-atmospheric CO_2 fluxes obscure the differentiation of urban-derived ΔXCO_2 signals from background CO_2 concentration in the rural areas. This limited generalizability can be in large part improved by leveraging the cooperative air sampling network of the National Oceanic and Atmospheric Administration (NOAA), which provide a range of remote marine stations for the developments of latitudinal references for background CO_2 concentration (Masarie and Tans, 1995; Tans et al., 1989). However, the continental-to-global spatial scales along multiple-site gradients of atmospheric background CO_2 (Mitchell et al., 2018) remain too coarse for precisely tracking background CO_2 dynamics in cities. This underscores the need for more spatially-explicit measurement techniques to better characterize subtle ΔXCO_2 variations within cities that contribute significant shares to global emissions (Duren and Miller, 2012).

To present both globally comprehensive and locally representative measurements of ΔXCO_2, we leverage a NASA's new Orbiting Carbon Observatory 3 (OCO-3) satellite that offers the state-of-the-art highest resolution observations ($\approx$ 3 km^2) covering the period from August 2019 to November 2023, and further remove atmospheric background CO_2 corrected from a novel global CO_2 baseline model based on ground-sourced CO_2 data from the Global Monitoring Laboratory (NOAA ESRL network). The satellite-derived dataset of global CO_2 enhancements enables objective, timely and spatially-explicit diagnosis of net impacts of CO_2 sources, sinks, and transport on atmospheric CO_2 increases, contributing to sub-city scale decision making on global net-zero strategies and climate actions.

2 Methods

This work develops a novel dataset of global CO_2 enhancements from 2019 to 2023 by integrating satellite-derived and ground-sourced CO_2 observations. Fig. 1 demonstrates the dataset involved and the main workflows. The following three subsections elaborate on carbon satellite XCO_2 product (XCO_2), the global CO_2 baseline estimation (CO_{2b}), and the global CO_2 enhancements (ΔXCO_2), respectively.

2.1 Satellite-retrieved XCO_2 Observations

Satellite-derived XCO_2 observations (column-averaged dry air mole fraction of CO_2; ppm) are from the Orbiting Carbon Observatory 3 (OCO-3). This NASA satellite, launched in 2019, collects the global magnitude and distribution of atmospheric CO_2 concentrations with the highest spatial-temporal resolution to date, allowing it to track XCO_2 variations with a grid resolution of 2.2×1.6 km^2. Studies have proven that the OCO-3 is capable of detecting localized emission sources by giving diurnal and geographically diverse XCO_2 observations (Kiel et al., 2021; Schwandner et al., 2017) and are less vulnerable to the impacts of small-scale atmospheric processes on the accuracy of local emission accounting (McKain et al., 2012). We use OCO-3 Level 2 bias-corrected XCO_2, version 10.4r data (OCO3_L2_Lite_FP), which is publicly available through the NASA Goddard Earth Science Data and Information Services Center (GES DISC) (http://disc.sci.gsfc.nasa.gov/). We filter the OCO-

https://doi.org/10.5194/essd-2025-234
Preprint. Discussion started: 17 June 2025

Open Access Earth System Science Data Discussions

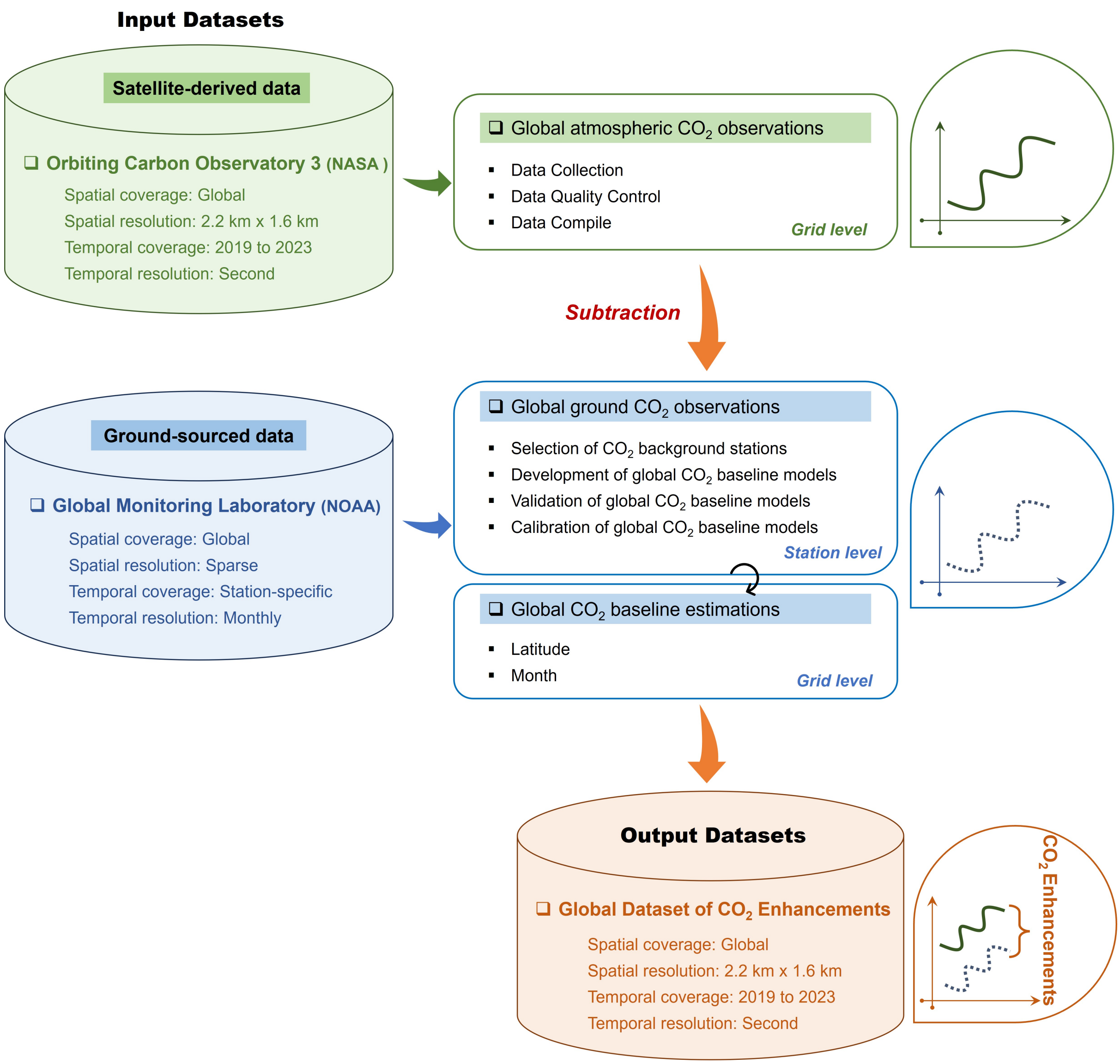

Fig. 1. A conceptual diagram of the generation process of the global CO_2 enhancements dataset.

https://doi.org/10.5194/essd-2025-234
Preprint. Discussion started: 17 June 2025

Table 1. The descriptive statistics of OCO-3 XCO_2 product.

Periods	Number of Observations	Mean (ppm)	1^{st} quantile (ppm)	99^{th} quantile (ppm)
2019-08 to 2019-12	3,807,526	408.49	402.39	413.67
2020-01 to 2020-12	15,045,735	411.52	405.17	416.70
2021-01 to 2021-12	13,526,529	414.17	408.36	419.57
2022-01 to 2022-12	12,383,251	416.44	409.86	421.94
2023-01 to 2023-11	9,685,130	418.49	412.58	424.02
Total	54,448,171	414.33	405.29	422.60

3 dataset using the 'Quality flag'. Quality flag 0 indicates high-quality remote-sensing data for scientific analysis. The full window of August 2019 through November 2023 with 90,714,334 XCO_2 samples is covered, of which, a total of 54,448,171 terrestrial observations are used for developing global XCO_2 dataset (Table 1).

2.2 Global CO_2 Baseline Estimation

2.2.1 Selection of global CO_2 background stations

Global Monitoring Laboratory (GML) within the Earth System Research Laboratories (ESRL) of NOAA operates a wide network of global ground-truth stations that accurately monitor long-term near-surface CO_2 levels. These stations are strategically deployed based on their geographical locations to represent background CO_2 concentrations.

The global CO_2 background stations are first required to be situated at considerable distances from urban infrastructures and anthropogenic activities to minimize human interference. Utilizing the global ESA Sentinel-2 10m land use/land cover map (Zanaga et al., 2022) to detect urban areas, we select monitoring stations that exhibit less than 2% built-up land cover within a radius of 5 kilometers (10×10 km^2 area). To further minimize local 'contamination' from dense vegetation, we additionally select stations with an Enhanced Vegetation Index (EVI) of less than 0.3 within the predefined box size, based on MODIS Vegetation Index Products (Didan, 2021). Moreover, sea-level flask samples are excluded to minimize the influence of air-ocean exchanges. This approach, different from NOAA's marine station selection (Conway and others, 1994), focuses exclusively on terrestrial sampling stations and provides enhanced representations of terrestrial CO_2 patterns. Stations situated within the Arctic and Antarctic circles, where carbon cycles exhibit unique characteristics (Bruhwiler et al., 2021), as well as those positioned downwind of emission sources, are similarly screened out. In addition, we conduct a visual inspection of the built-up surfaces and vegetation characteristics within a 5-km buffer zone around each monitoring station to avoid misguidance in station selection due to local heterogeneity. This examination is especially crucial for island stations, which often lack detailed land use and vegetation cover data. On this basis, we exclude stations with nearby vegetation or built-up areas, even if these are minimal within the buffer zone. In accordance with baseline modelling requirements, we ensure that the selected background stations have CO_2 time series data for at least 10 years between 2000 and 2023.

https://doi.org/10.5194/essd-2025-234
Preprint. Discussion started: 17 June 2025

Open Access Earth System Science Data Discussions

Of the 88 active sites across 38 countries from the Global Monitoring Laboratory (NOAA ESRL network), a total of eight CO_2 background stations with wide latitudinal and longitudinal coverage (Fig. 2, Table 2) are chosen to model the global CO_2 baseline.

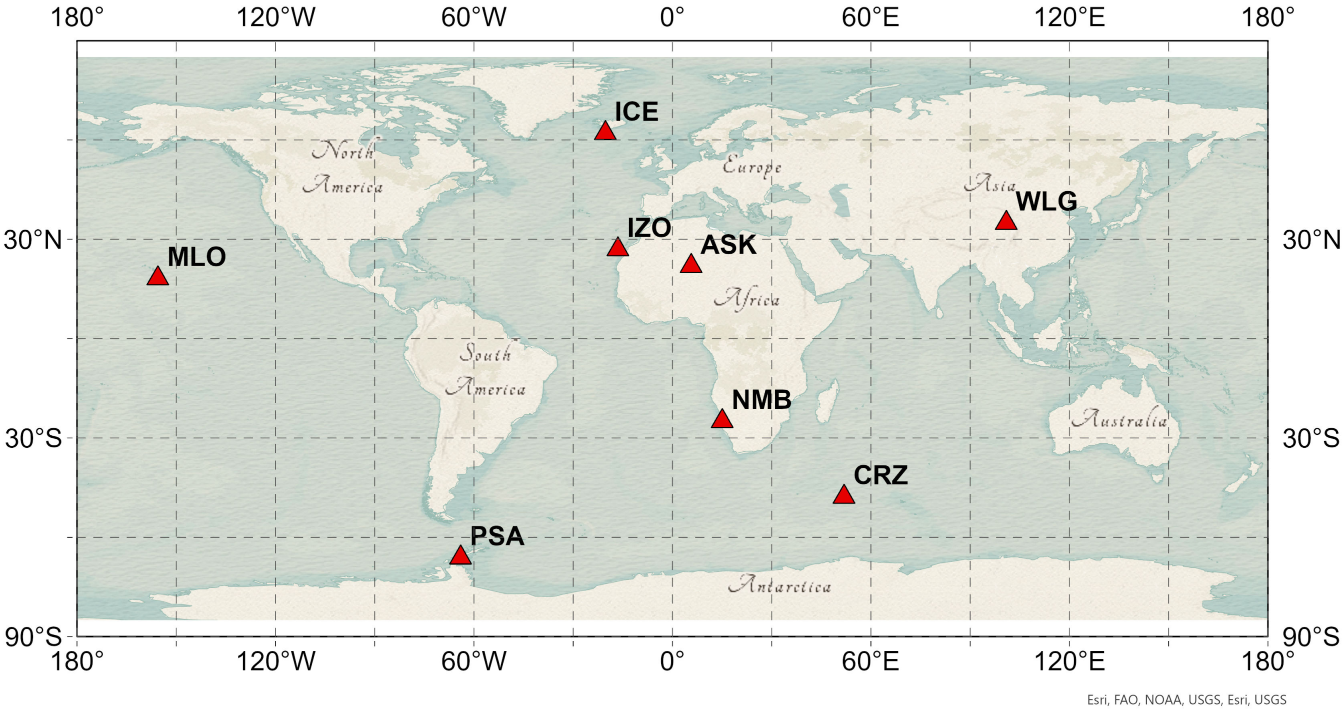

Fig. 2. The locations of eight CO_2 background stations. Station codes and names are highlighted in bold, including ICE: Storhofdi, Vestmannaeyjar; WLG: Mt.Waliguan; IZO: Izana, Tenerife, Canary Islands; ASK: Assekrem; MLO: Mauna Loa, Hawaii; NMB: Gobabeb; CRZ: Crozet Island; PSA: Palmer Station, Antarctica. Sources of Basemap: Esri, TomTom, Garmin, FAO, NOAA, USGS, © OpenStreetMap contributors, and the GIS User Community.

2.2.2 Development of a global CO_2 baseline model

We construct a global model to estimate spatio-temporal CO_2 baseline (CO_{2b}) using a simple and interpretable near-sinusoidal growth function (Eq.1). The mathematical form is an addition of a sinusoidal function and a linear function, both depending on a time parameter, m, denoting the number of months since January 2000. While the sinusoidal function simulates the wave-like periodicity and oscillation of seasonal CO_2 swings caused by seasonal changes in ecosystem photosynthesis and respiration (Arrigo et al., 1987; Hall et al., 1975), the linear function simulates the long-term trend of atmospheric CO_2 concentration, which has been documented for decades (Groves et al., 1978). $\pi/6$ is the unit angle of one month in the sinusoidal function. f is the frequency of CO_2 seasonal variations. ϕ_h signifies the phase shift due to the inconsistent interhemispheric seasonality. ϵ_h denotes a residual term. h can be North or South Hemisphere.

https://doi.org/10.5194/essd-2025-234
Preprint. Discussion started: 17 June 2025

Table 2. The location, percentages of built-up area, vegetation greenness, and satellite images of CO_2 background stations. The red triangles are the locations of background stations. Source: Google Maps (© Google, accessed July 11, 2024)

Station	Location	Built-up Percentage (%)	Average EVI	Data Range	Satellite Images
ICE	63.400°North, 20.288°West	0.00	0.14	1992-2023	
WLG	36.288°North, 100.896°East	0.00	0.21	1990-2023	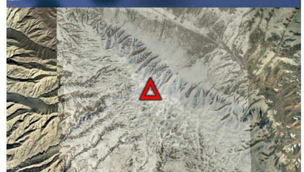
IZO	28.309°North, 16.499°West	0.31	0.17	1991-2023	
ASK	23.263°North, 5.632°East	0.00	0.05	1995-2023	
MLO	19.536°North, 155.576°West	0.00	0.00	1969-2023	
NMB	23.580°South, 15.030°East	0.23	0.07	1997-2023	
CRZ	46.434°South, 51.848°East	0.02	0.21	1991-2023	
PSA	64.774°South, 64.053°West	0.00	NoData	1978-2023	

https://doi.org/10.5194/essd-2025-234
Preprint. Discussion started: 17 June 2025

Further, we allow parameters, $\beta_{2,h}$, $\beta_{1,h}$, and $\beta_{0,h}$, in Eq.1 to be linearly dependent on latitude, l (Eq.2), considering that latitudinal gradient exerts considerable influence on human activities (Lei et al., 2021), naturally terrestrial biota, and air transmission through the troposphere (Denning et al., 1995) and thereby affecting the spatiotemporal distributions of CO_2 baseline levels (Conway and Tans, 1999; Shim et al., 2013). Specifically, studies reported a non-linear latitude dependence of seasonal CO_2 amplitude from the South Pole to the North Pole (Yun et al., 2022; Forkel et al., 2016; Heimann et al., 1998). The seasonal CO_2 amplitude varies slightly with latitude in the South Hemisphere whereas it shows a reinforced trend at high latitudes in the North Hemisphere. The growth rate of atmospheric CO_2 is also sensitive to latitude (Taylor and Orr, 2000). $\beta_{0,h}(l)$ represents the latitude-dependent prehistoric CO_2 concentration. In addition, Eq.3 ensures that baseline estimations in the North and South Hemispheres are continuous at the equator.

$$CO_{2b,h}(l,m) = \beta_{2,h}(l)\cdot\sin(\frac{\pi}{6}\cdot m\cdot f+\phi_h)+\beta_{1,h}(l)\cdot m+\beta_{0,h}(l)+\epsilon_h, \quad h\in\{south, north\} \tag{1}$$

$$\beta_{i,h}(l) = \beta_{1,i,h}\cdot l+\beta_{0,i,h}+\epsilon_{i,h}, \quad i\in\{0,1,2\} \tag{2}$$

$$\text{subject to, } CO_{2b,south}(0,m) = CO_{2b,north}(0,m) \tag{3}$$

The global CO_2 baseline model is constructed using 2,097 monthly observations collected between 2000 and 2023 from eight selected CO_2 background stations. This model has achieved near-perfect goodness-of-fit with R^2=0.988 and RMSE=1.78 for North-Hemisphere curves, and R^2=0.995 and RMSE=1.09 for South-Hemisphere curves. Fig. 3 illustrates time-series CO_2 observations and estimations at eight CO_2 background stations. For model simplicity, the student's t-test are applied to examine the statistical significance of all model parameters and only the significant ones (p-value < 0.05) remain in the final model. Eq.4 and 5 represent estimated CO_2 baseline models respectively for the North and South Hemispheres. These should be able to offer accurate estimates of CO_2 baseline levels at any latitude without being constrained by ground-truth station layout.

$$CO_{2b,north} = -0.625\cdot\sin(\frac{\pi}{6}\cdot m\cdot 1.002+0.846)+0.129\cdot l\cdot\sin(\frac{\pi}{6}\cdot m\cdot 1.002)+0.186\cdot m+0.035\cdot l+366.240 \tag{4}$$

$$CO_{2b,south} = -0.625\cdot\sin(\frac{\pi}{6}\cdot m\cdot 1.002+0.846)+(1.180e^{-4}\cdot l+0.186)\cdot m+0.027\cdot l+366.240 \tag{5}$$

$$CO_{2b}(0,m) = -0.625\cdot\sin(\frac{\pi}{6}\cdot m\cdot 1.002+0.846)+0.186\cdot m+366.240 \tag{6}$$

2.2.3 Sensitivity Analysis

Parameter sensitivity analysis is performed to examine the robustness of the developed global CO_2 baseline model over different criteria for background station selection. Multi-criteria combinations of the percentage of built-up areas, the EVI-based vegetation greenness, and buffer size of background stations are used for this purpose. By setting the thresholds of built-up percentages at 2% and 5%, the thresholds of EVI values at 0.2 and 0.3, and the thresholds of buffer radius at 2.5 km and 5.0 km, we compare the selected CO_2 background stations and their fitting performances. The background CO_2 estimations are highly stable and not sensitive to changes in background station selection criteria (Table 3).

https://doi.org/10.5194/essd-2025-234
Preprint. Discussion started: 17 June 2025

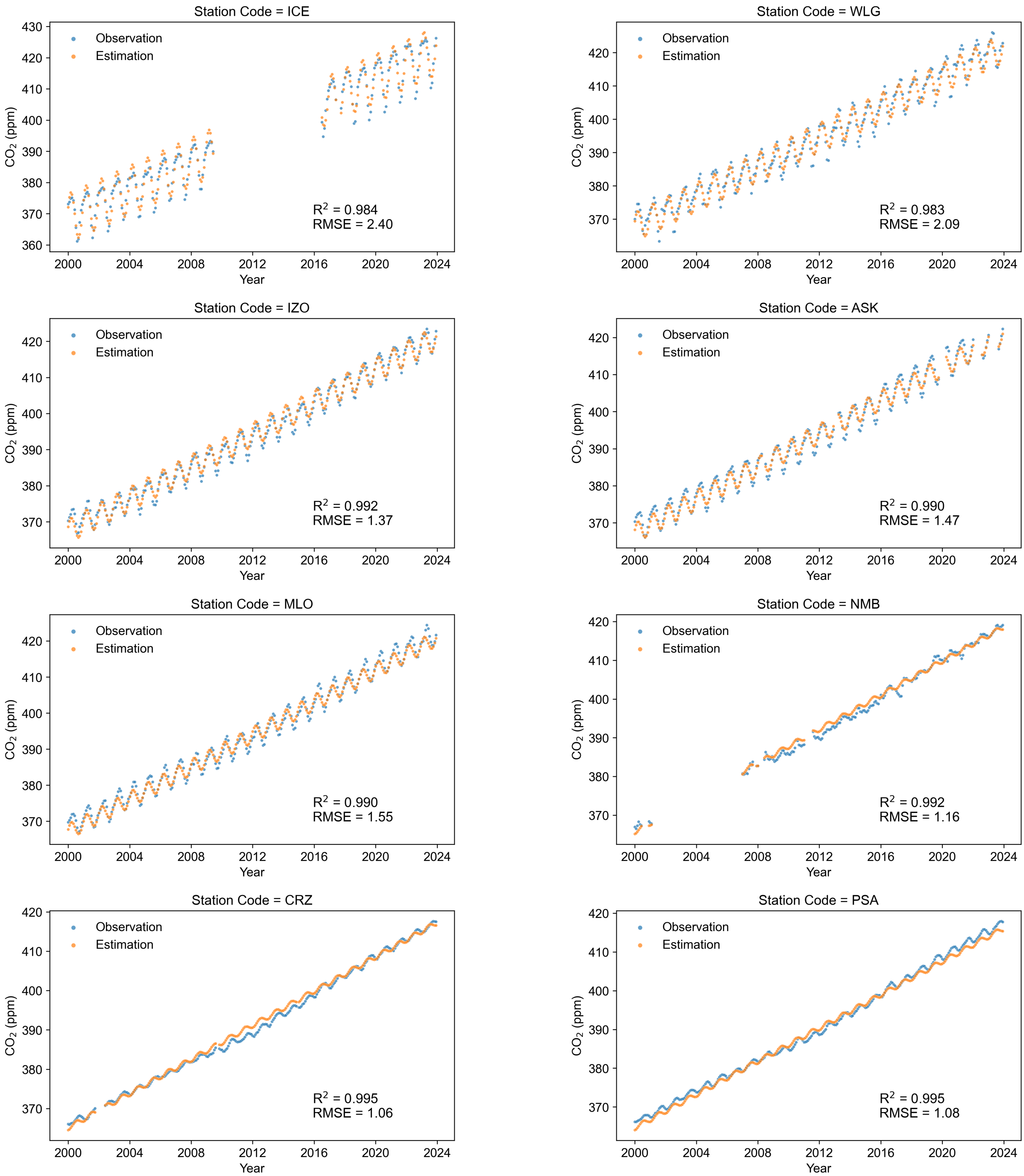

Fig. 3. The performance of the developed global CO_2 baseline model at eight CO_2 background stations.

https://doi.org/10.5194/essd-2025-234
Preprint. Discussion started: 17 June 2025

Table 3. The sensitivity test of the estimated global CO_2 baseline model

Buffer Radius: 2.5 km		
Built-up Percentage (%)	Average EVI	Model Performance
< 2%	< 0.2	North Hemisphere Model: R^2=0.989; RMSE=1.67
		South Hemisphere Model: R^2=0.994; RMSE=1.10
< 5%	< 0.2	North Hemisphere Model: R^2=0.989; RMSE=1.67
		South Hemisphere Model: R^2=0.994; RMSE=1.10
< 2%	< 0.3	North Hemisphere Model: R^2=0.988; RMSE=1.78
		South Hemisphere Model: R^2=0.995; RMSE=1.09
< 5%	< 0.3	North Hemisphere Model: R^2=0.986; RMSE=1.88
		South Hemisphere Model: R^2=0.994; RMSE=1.10
Buffer Radius: 5.0 km		
Built-up Percentage (%)	Average EVI	Model Performance
< 2%	< 0.2	North Hemisphere Model: R^2=0.989; RMSE=1.67
		South Hemisphere Model: R^2=0.994; RMSE=1.10
< 5%	< 0.2	North Hemisphere Model: R^2=0.989; RMSE=1.67
		South Hemisphere Model: R^2=0.994; RMSE=1.10
< 2%	< 0.3	North Hemisphere Model: R^2=0.988; RMSE=1.78
		South Hemisphere Model: R^2=0.995; RMSE=1.09
< 5%	< 0.3	North Hemisphere Model: R^2=0.988; RMSE=1.78
		South Hemisphere Model: R^2=0.995; RMSE=1.09

2.3 A global dataset of CO_2 enhancements

The CO_2 enhancements, ΔXCO_2, is estimated as the difference between remote-sensing CO_2 observations (XCO_2) and a column-average concentration equivalent of the CO_2 baseline (XCO_{2b}) (Eq.7), considering the vertical profile of atmospheric CO_2 by altitude (Bischof et al., 1980). We derived XCO_{2b} by applying a linear calibration function to CO_{2b}, based on 28,397 co-located observations from OCO-3 and CO_2 background stations (R^2=0.909). The calibration function, with both its coefficients and constant terms linearly dependent on latitude due to the sensitivity of atmospheric vertical mixing and circulation to latitude changes (Monte-carlo and Sun, 1985; Huth et al., 2008), can scale ground-sourced CO_2 observations to satellite-based column average concentration.

$$\Delta \mathrm{XCO}_2 = XCO_2 - XCO_{2b} \quad (7)$$

https://doi.org/10.5194/essd-2025-234
Preprint. Discussion started: 17 June 2025

3 Dataset description

This study develops a cutting-edge dataset featuring instantaneous and highest-resolution (≈ 3 km^2) estimates of global CO_2 enhancements, which contains 54,448,171 ΔXCO_2 observations across terrestrial regions (between approximately 52.88°S and 53.58°N) from August 2019 to November 2023. Of them, 1,231,856 ΔXCO_2 samples locate in urban areas, as defined by a published global urban extents map (Zhao et al., 2022). The dataset's high spatiotemporal resolution enables precise detection of short-term CO_2 enhancements driven by human activities and natural processes. For long-term evolution of atmospheric CO_2 burden, monthly or annual aggregations are recommended.

However, the spatio-temporal coverage of ΔXCO_2 is incomplete owing to OCO-3 observations loss attributed to cloud coverage and other data quality issues (Table. 1). Users are advised to examine the data coverage within their specific study area. Efforts are underway to mitigate this problem leveraging spatio-temporal interpolation techniques (Wu et al., 2024). Ongoing improvements of dataset coverage are expected as OCO-3 observations accumulate. A future work will involve cross-verifying background CO_2 estimates at a regional scale to ensure the consistency and accuracy of baseline models at different spatial resolutions.

The global dataset of CO_2 enhancements is stored in a NetCDF file with data attributes including latitude, longitude, time, satellite-derived CO_2, and CO_2 enhancements. At the time of writing this article, this dataset has been updated to November 2023. Future updates will also be available alongside with newly available OCO-3 data and NOAA ESRL station data.

4 Results and discussion

4.1 Dataset validation

4.1.1 Validation against tropospheric NO_2 measurements

The validation of this developed CO_2 enhancements dataset is performed by comparing ΔXCO_2 values in urban areas with co-located tropospheric NO_2 columns. This is a well-accepted approach because of the CO_2-NO_x co-emission (Dou et al., 2023; Huo et al., 2022; Lei et al., 2022). Due to its shorter lifetime (hours), NO_2 is less affected by long-distance atmospheric transport, making it easier to be detected (Reuter et al., 2014; Richter et al., 2005). It means that the NO_2 column variation can trace the enhanced urban CO_2 compared to the global baseline due to human activities or natural processes (Wang et al., 2020). This study uses the Sentinel-5P TROPOMI Tropospheric NO_2 L2 product (https://disc.gsfc.nasa.gov/), which provides the tropospheric NO_2 column measures at a spatial resolution of 3.5×5.5 km^2. Observations with a quality assurance (qa) value higher than 0.75 are utilized here to ensure trustworthiness. We geospatially match the hourly ΔXCO_2 samples and the co-located NO_2 observed throughout the three-hour window covering one hour before and one hour after the specified hour of the day. We also perform aggregation by averaging the ΔXCO_2 values within the NO_2 grids. Since the NO_2 data is coarser than our dataset, we only use NO_2 grids that have at least three ΔXCO_2 observations to illustrate the relationship

https://doi.org/10.5194/essd-2025-234
Preprint. Discussion started: 17 June 2025

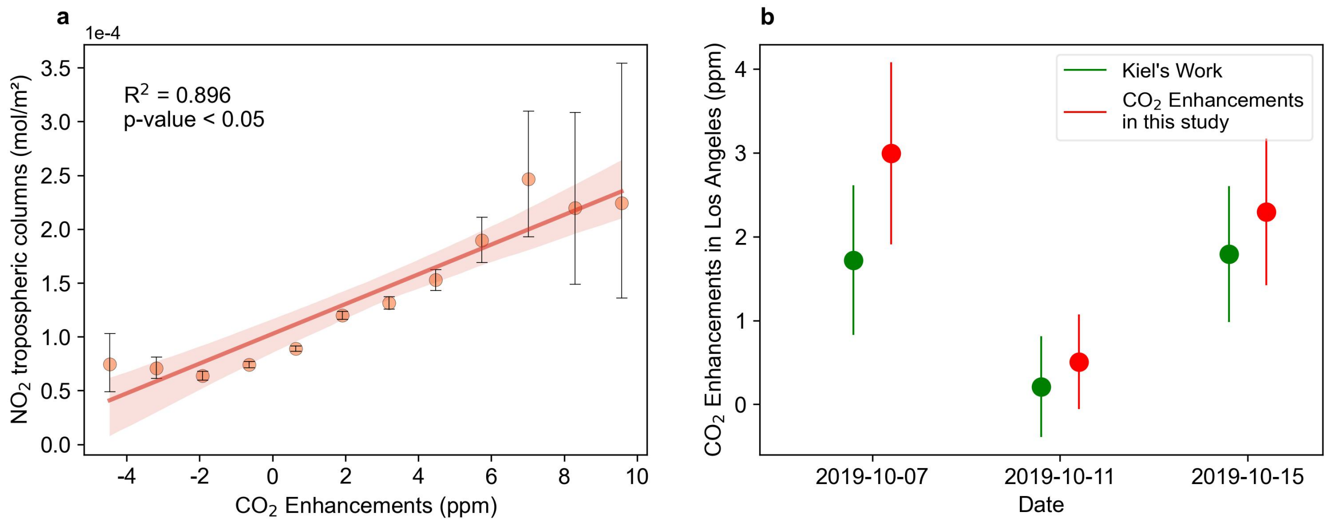

Fig. 4. Validation of global CO_2 enhancements (ΔXCO_2). (a) Relationship between the binned ΔXCO_2 and co-located average NO_2 values in built-up areas worldwide. The error bar denotes the 95% Confidence Interval. (b) Compare the hourly ΔXCO_2 on three days in Los Angeles with a previous study (Kiel et al., 2021). The error bar denotes standard deviations.

between binned ΔXCO_2 and average NO_2 values. Using ΔXCO_2 samples from global built-up regions, we confirm a strong correlation between the proposed CO_2 enhancements and NO_2 values, with R^2=0.896 (Fig. 4a).

4.1.2 Comparison with existing urban CO_2 enhancements

We also compare ΔXCO_2 data proposed in this article with a previous urban CO_2 enhancements paper focusing on the Los Angeles megacity which measured background concentration using a remote surface station (Kiel et al., 2021). Kiel et al. (2021) reported intra-urban enhanced CO_2 relative to the background CO_2 for specific one hour on four days. To mitigate the wind impacts on locally atmospheric CO_2, only urban CO_2 observations from three of those days are compared (Fig. 4b). We find that the hourly ΔXCO_2 estimates provided by our datasets align closely with those reported in Kiel et al. (2021). The Mann-Whitney U test, with a p-value of 0.4, indicates insignificant difference between the ΔXCO_2 averages of two datasets. This suggests a great agreement between our CO_2 enhancements dataset and prior works.

4.2 Spatial patterns of global CO_2 enhancements

Fig.5a illustrates the spatial distributions of global ΔXCO_2 measurements aggregated to 2°×2° grids. From 2019 to 2023, the global land exhibits ΔXCO_2 ranging from -49.86 ppm to 21.25 ppm with an average of 0.58 ppm and a standard deviation of 1.81 ppm (Fig. 5b). North Hemisphere shows an average ΔXCO_2 at 0.67 ppm (std=1.98), which is approximately 81% higher than the average ΔXCO_2 of 0.37 ppm observed in the South Hemisphere (std=1.32) (Fig. 5b). We note that major CO_2 enhancements are concentrated in Eastern and South-Eastern Asia as well as equatorial tropical forests (e.g., Indonesia

https://doi.org/10.5194/essd-2025-234
Preprint. Discussion started: 17 June 2025

forest cover and tropical savannahs) (Fig. 5a). High ΔXCO_2 levels in Eastern and South-Eastern Asia are primarily driven by anthropogenic factors including accelerated socioeconomic development and population growth. In contrast, the elevated ΔXCO_2 near the equator can be attributed to biospheric factors. First, frequent fires in the tropical savannahs of the Sahel-Sudano-Guinean region emit substantial amounts of CO_2 into the atmosphere (Van Der Werf et al., 2017), Second, tropical woody vegetation increasingly functions as net carbon sources due to degradation and deforestation (Baccini et al., 2017).

With fine spatio-temporal resolution, the global dataset of CO_2 enhancements also provides detailed information for monitoring and characterizing ΔXCO_2 within urban areas. There are significant heterogeneity in urban ΔXCO_2 levels across six continents (Fig. 6a). North America has the highest average (mean = 1.76 ppm; std = 2.04 ppm), displaying relatively lower ΔXCO_2 in the east than the west, because larger quantities of plants in the east absorb atmospheric CO_2 and attenuate the ΔXCO_2 levels. Asia follows, with an average of 1.72 ppm and a standard deviation of 2.08 ppm. By comparison, Oceania has the lowest ΔXCO_2 levels, averaging 0.59 ppm (std = 1.27 ppm) from 2019 to 2023.

The ΔXCO_2 values observed in global urban areas range from -16.89 ppm to 18.66 ppm with an average approximation of 1.43 ppm and a standard deviation of 2.04 ppm (Fig. 6b). The urban average ΔXCO_2 worldwide being roughly 1.5 times higher than the global terrestrial mean highlights the significant influence of urban environments on the rise of atmospheric CO_2 levels. Urban areas in the North Hemisphere have an average ΔXCO_2 of 1.52 ppm, about 95% higher than the average level in the counterparts of South Hemisphere (Fig. 6c-d), owing to populated city distributions in the North. Fig. 7 exemplifies the spatial maps of ΔXCO_2 across six global cities. The spatially-explicit ΔXCO_2 values at sub-city scale have been clearly depicted and varying ΔXCO_2 levels between urban areas are also shown.

4.3 Temporal dynamics of global CO_2 enhancements

The temporal patterns of global CO_2 enhancements differ between the North and South Hemispheres, both in terms of changes in monthly ΔXCO_2 averages and in their seasonal variability. In the North Hemisphere, the monthly trend of ΔXCO_2 mean has a statistically significant increase (p-value<0.05 tested by a linear least-squares regression) from 2019 to 2023 with a slope of roughly 0.03 ppm per month (R^2=0.31). Within North hemisphere urban areas, the monthly ΔXCO_2 mean increases approximately 0.04 ppm per month (R^2=0.33) (Fig. 8a). No notable trend in the monthly ΔXCO_2 averages has been detected in the South Hemisphere and its urban areas (Fig. 8b). Moreover, the North Hemisphere, regardless of terrestrial land or urban coverage, experiences more pronounced seasonal fluctuations compared to the South Hemisphere which has lower terrestrial vegetation biomass.

Seasonal disparities in average ΔXCO_2 are evident (Fig. 8c), with the highest average (mean = 1.05 ppm) occurring in autumn in which terrestrial ecosystem increases net carbon release due to stronger total ecosystem respiration relative to gross primary productivity (Tang et al., 2022; Piao et al., 2008). In contrast, spring experiences the lowest average ΔXCO_2 (mean = 0.02 ppm) because of the onset of growing season and reduced human heating and cooling demands (Shen et al., 2014). Human cooling- and heating-caused CO_2 emissions explain the increases in averaged ΔXCO_2 during summer (mean = 0.67 ppm) and winter (mean = 0.40 ppm), respectively, compared to spring.

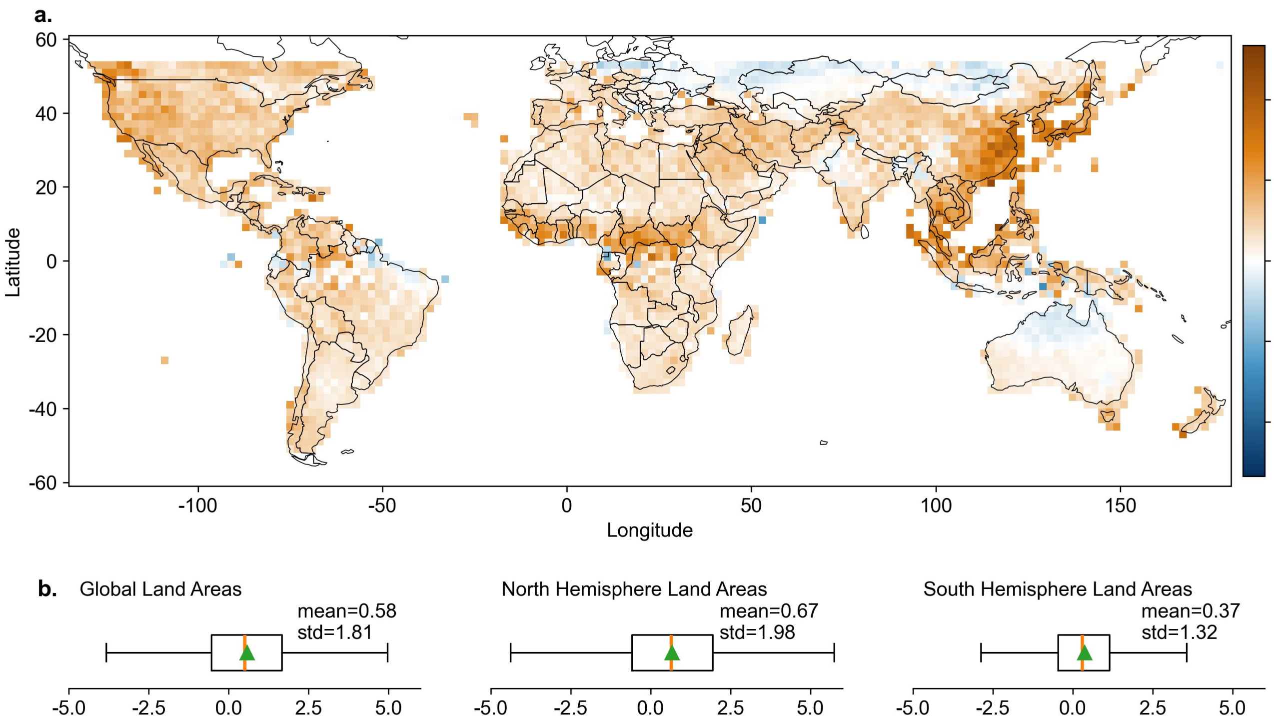

Fig. 5. The spatial map of CO_2 enhancements (ΔXCO_2) in global land areas at grids of 2° latitude by 2° longitude for illustration purpose (a). The box-plots display the ΔXCO_2 distributions at the original resolution (2.2×1.6 km^2) across land areas globally, as well as within the North and South Hemisphere (b). The 'whiskers' of box-plots extend to 1.5 times the Interquartile Range (IQR) from Q1 and Q3, and outliers are hidden. The green triangle denotes the mean value and the orange line signifies the median value.

5 Conclusions

We generate a global dataset of CO_2 enhancements relative to the long-term CO_2 baseline, intending to identify ways that satellite-derived retrievals can guide local net-zero target and to foster international partnerships toward achieving carbon neutrality. Through synergistic integration of satellite-derived and ground-sourced CO_2 observations, this dataset provides 54,448,171 and 1,231,856 ΔXCO_2 records in global land areas and global urban areas over 2019-2023, respectively, with high spatial (≈ 3 km^2) and temporal (instantaneous) resolutions. The spatiotemporal patterns also reveal that this CO_2 enhancements dataset is capable of capturing and characterizing the variability in net effects of carbon sources, sinks, and atmospheric transport on atmospheric CO_2 increases, across the globe and down to minimal intra-city scale.

The core strength of this dataset is to deliver spatially-explicit maps that enable instantaneous monitoring and ensure continuous, equitable tracking of CO_2 enhancements at multiple scales (across continents, countries, and cities). By identifying hot-spots and diagnosing temporal trends via a standardized metric, it equips international and domestic policy-makers with

https://doi.org/10.5194/essd-2025-234
Preprint. Discussion started: 17 June 2025

Open Access Earth System Science Data Discussions

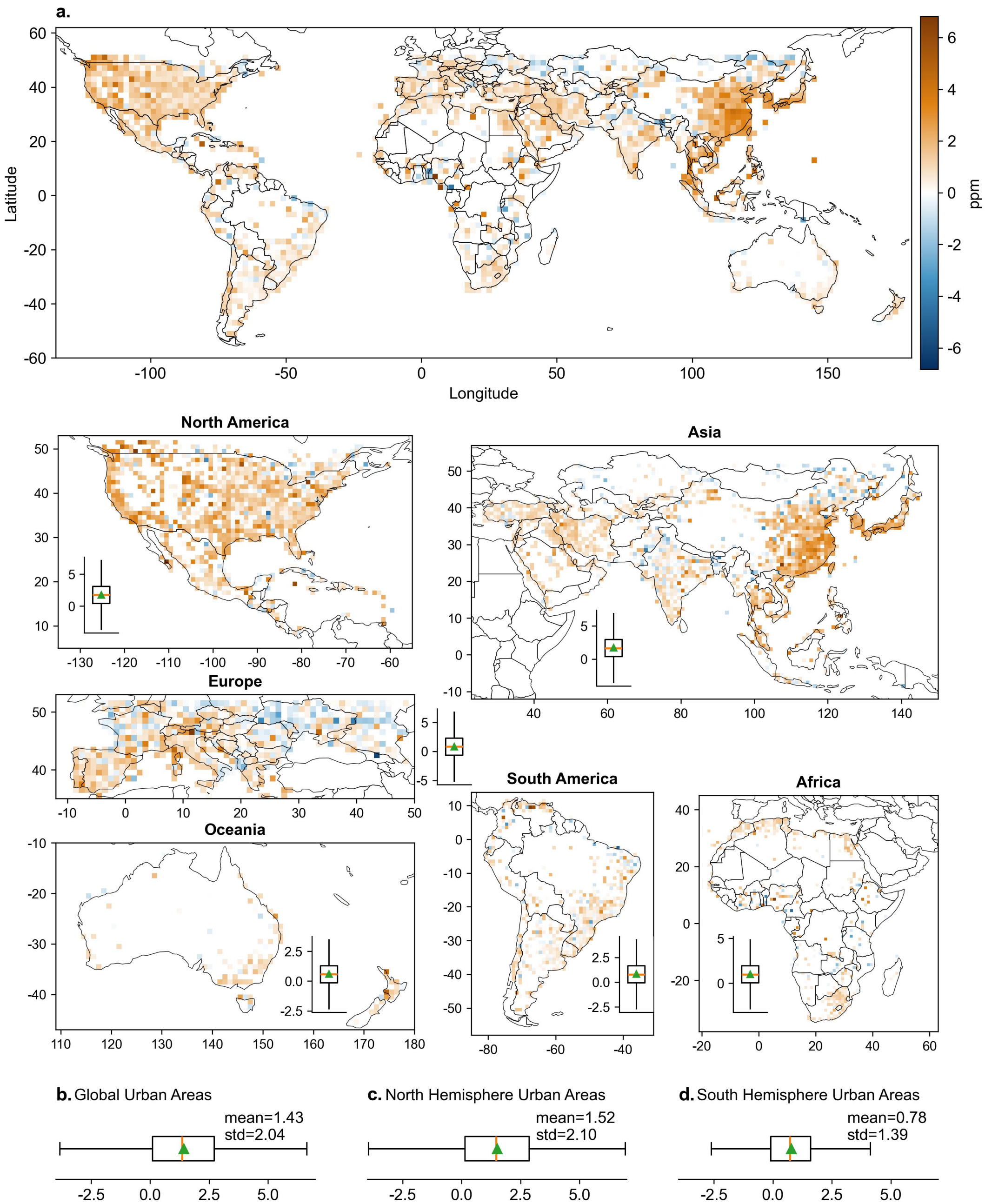

Fig. 6. The spatial maps of CO_2 enhancements (ΔXCO_2) throughout global urban areas (2°×2°) and six regions (1°×1°) (a). The ΔXCO_2 distributions within urban areas are presented for the global scale (b), the North Hemisphere (c), and the South Hemisphere (d). The 'whiskers' of box-plots extend to 1.5 times the Interquartile Range (IQR) from Q1 and Q3, and outliers are hidden. The green triangle denotes the mean value and the orange line signifies the median value.

Open Access Earth System Science Data Discussions

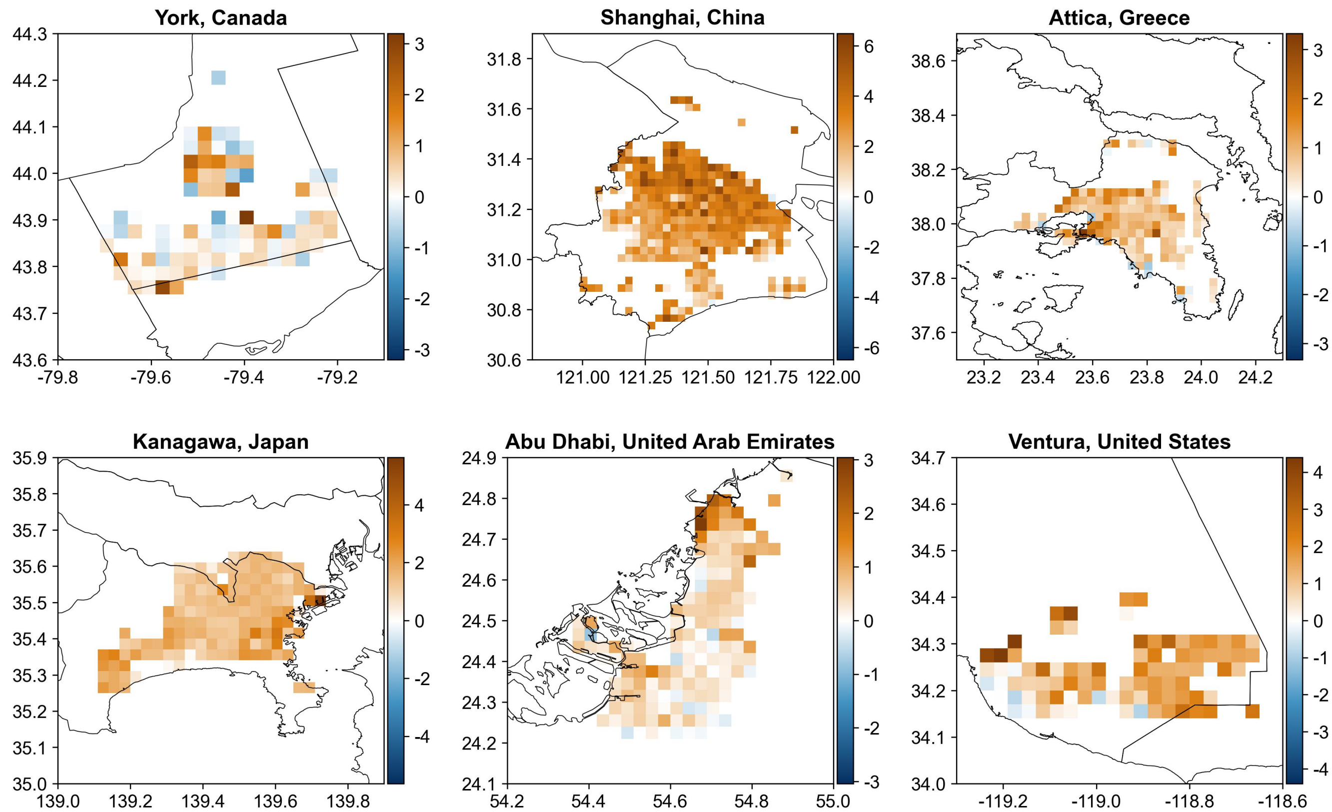

Fig. 7. The spatial maps of CO_2 enhancements (ΔXCO_2) of six global cities aggregated to 0.02° resolution grids.

evidence-based insights. This will support the development of targeted and well-informed strategies for hierarchical carbon governance, and ultimately enhancing effective responses to climate risks.

6 Data availability

The global dataset of CO_2 enhancements is freely available at https://doi.org/10.5281/zenodo.15209825 (Zhou et al., 2025). This dataset has been organized in NetCDF format under the WGS84 geographic coordinate system. It is compatible with Python, R, and free GIS software for reading and post-processing. As the satellite-derived and ground-sourced CO_2 observations update, the dataset will be continuously released aiming to consistently support in global carbon management and climate change mitigation.

https://doi.org/10.5194/essd-2025-234
Preprint. Discussion started: 17 June 2025

Open Access Earth System Science Data Discussions

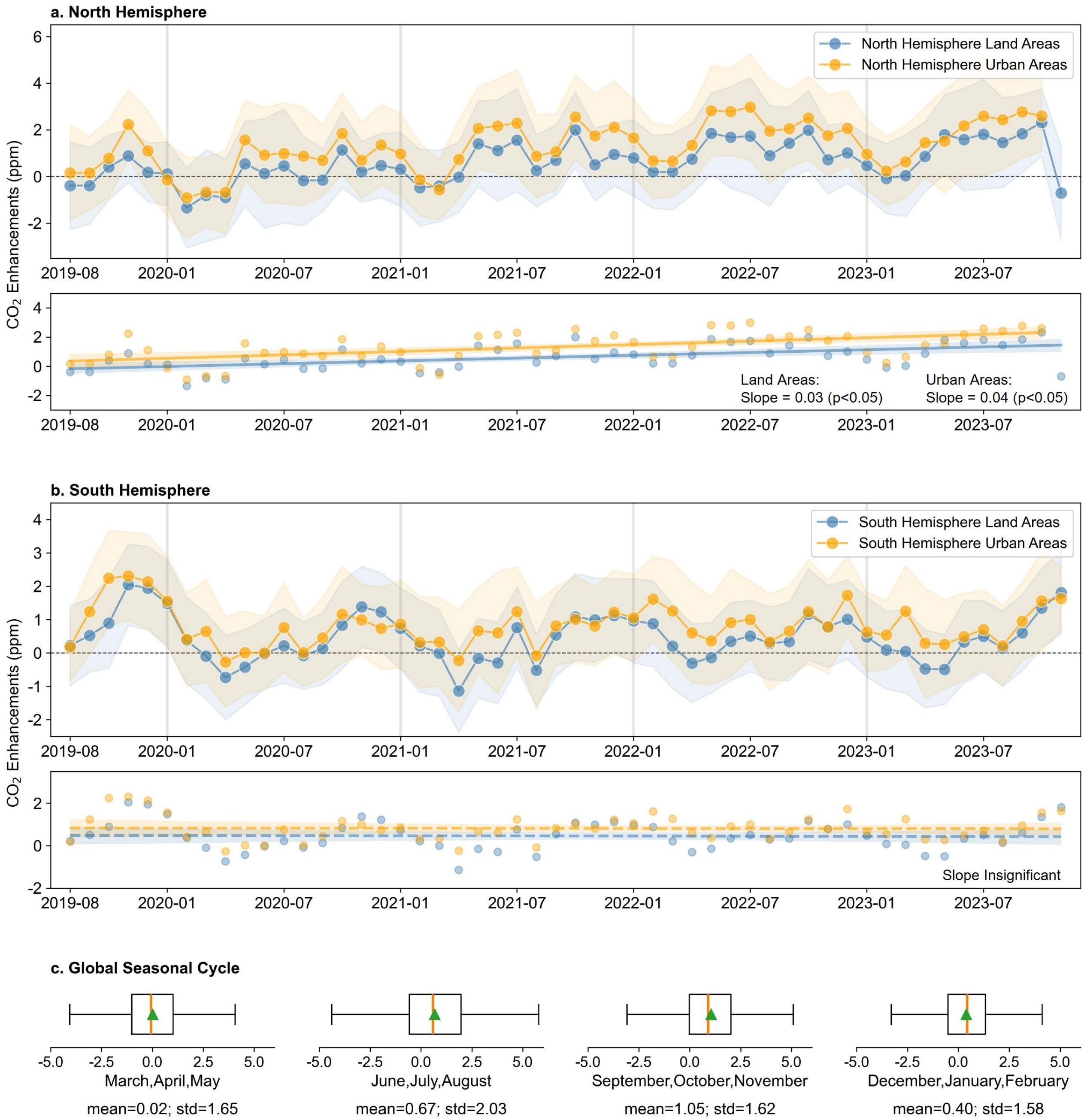

Fig. 8. The monthly variations of CO_2 enhancements (ΔXCO_2) in the North Hemisphere (a) and South Hemisphere (b). The monthly mean ΔXCO_2 values exhibit statistically significant upward trend over land and urban areas in the North Hemisphere (p-value<0.05) whereas no significant trend is observed in the South Hemisphere. Global seasonal cycles of CO_2 enhancements are shown at (c). The 'whiskers' of box-plots extend to 1.5 times the Interquartile Range (IQR) from Q1 and Q3, and outliers are hidden. The green triangle denotes the mean value and the orange line signifies the median value.

https://doi.org/10.5194/essd-2025-234
Preprint. Discussion started: 17 June 2025

Author contributions. Y.Z. conceptualized the data product and supervised the project. P.F. and Y.Z. designed methodology, analyzed data, and wrote the manuscript. J.L. and Y.X. contributed to methodological design and manuscript editing. B.H. and C.W. contributed to conceptualization and manuscript editing.

Competing interests. The authors declare no competing interests.

Acknowledgements. This study is funded by National Key Research and Development Program of China (2022YFB3903704). J.L. acknowledges the funding from USMILE European Research Council (ERC CU18-3746). B.H. acknowledges the Senior Research Fellow Scheme from the Hong Kong Research Grants Council (SRFS2324-4H02).

https://doi.org/10.5194/essd-2025-234
Preprint. Discussion started: 17 June 2025

References

Arrigo, R. D., Jacoby, G. C., and Fung, I. Y.: Boreal forests and atmosphere-biosphere exchange of carbon dioxide, Nature, 329, 321–323, 1987.

Baccini, A., Walker, W., Carvalho, L., Farina, M., and Houghton, R. A.: Tropical forests are a net carbon source based on aboveground measurements of gain and loss, Science, 358, 230–234, https://doi.org/10.1126/science.aat1205, 2017.

Bischof, W., Fabian, P., and Borchers, R.: Decrease in CO2 mixing ratio observed in the stratosphere, Nature, 288, 347–348, 1980.

Bruhwiler, L., Parmentier, F.-J. W., Crill, P., Leonard, M., and Palmer, P. I.: The Arctic Carbon Cycle and Its Response to Changing Climate, Current Climate Change Reports, 7, 14–34, https://doi.org/10.1007/s40641-020-00169-5/Published, 2021.

Canadell, J. G., Monteiro, P. M., Costa, M. H., Cotrim da Cunha, L., Cox, P. M., Eliseev, A. V., and Zickfeld, K.: Global Carbon and Other Biogeochemical Cycles and Feedbacks, in: Climate change 2021: The physical science basis. Contribution of working group I to the sixth assessment report of the intergovernmental panel on climate change (pp. 673-816)., pp. 673–816, Cambridge University Press, https://doi.org/10.1017/9781009157896.007, 2023.

Che, K., Lauvaux, T., Taquet, N., Stremme, W., Xu, Y., Alberti, C., Lopez, M., García-Reynoso, A., Ciais, P., Liu, Y., Ramonet, M., and Grutter, M.: Urban XCO2 Gradients From a Dense Network of Solar Absorption Spectrometers and OCO-3 Over Mexico City, Journal of Geophysical Research: Atmospheres, 129, e2023JD040 063, https://doi.org/10.1029/2023JD040063, 2024.

Conway, T. J. et al.: Evidence for interannual variability of the carbon cycle from the National Oceanic and Atmospheric Administration/-Climate Monitoring and Diagnostics Laboratory Global Air Sampling Network, Journal of Geophysical Research, 99, 22,831–22,855, https://doi.org/10.1029/94jd01951, 1994.

Conway, T. J. and Tans, P. P.: Development of the CO2 latitude gradient in recent decades, Global Biogeochemical Cycles, 13, 821–826, https://doi.org/10.1029/1999GB900045, 1999.

Denning, A. S., Fungt, I. Y., and Randall, D.: Latitudinal gradient of atmospheric CO2 due to seasonal exchange with land biota, Nature, 376, 240–243, 1995.

Didan, K.: MODIS/Terra Vegetation Indices Monthly L3 Global 1km SIN Grid V061, https://doi.org/10.5067/MODIS/MOD13A3.061, 2021.

Dou, X., Hong, J., Ciais, P., Chevallier, F., Yan, F., Yu, Y., Hu, Y., Huo, D., Sun, Y., Wang, Y., Davis, S. J., Crippa, M., Janssens-Maenhout, G., Guizzardi, D., Solazzo, E., Lin, X., Song, X., Zhu, B., Cui, D., Ke, P., Wang, H., Zhou, W., Huang, X., Deng, Z., and Liu, Z.: Near-real-time global gridded daily CO2 emissions 2021, Scientific data, 10, 69, https://doi.org/10.1038/s41597-023-01963-0, 2023.

Duren, R. M. and Miller, C. E.: Measuring the carbon emissions of megacities, Nature Climate Change, 2, 560–562, https://doi.org/10.1038/nclimate1629, 2012.

Forkel, M., Carvalhais, N., Rödenbeck, C., Keeling, R., Heimann, M., Thonicke, K., Zaehle, S., and Reichstein, M.: Enhanced seasonal CO2 exchange caused by amplified plant productivity in northern ecosystems, Science, 351, 696–699, https://doi.org/10.1126/SCIENCE.AAC4971, 2016.

Groves, K. S., Mattingly, S. R., and Tuck, A. F.: Increased atmospheric carbon dioxide and stratospheric ozone, Nature, 273, 1978.

Hakkarainen, J., Ialongo, I., and Tamminen, J.: Direct space-based observations of anthropogenic CO2 emission areas from OCO-2, Geophysical Research Letters, 43, 11,400–11,406, https://doi.org/10.1002/2016GL070885, 2016.

Hakkarainen, J., Ialongo, I., Maksyutov, S., and Crisp, D.: Analysis of Four Years of Global XCO2 Anomalies as Seen by Orbiting Carbon Observatory-2, Remote Sensing, 11, 850, https://doi.org/10.3390/RS11070850, 2019.

https://doi.org/10.5194/essd-2025-234
Preprint. Discussion started: 17 June 2025

Hall, C. A., Ekdahl, C. A., and Wartenberg, D. E.: A fifteen-year record of biotic metabolism in the Northern Hemisphere, Nature, 255, 136–138, 1975.

Heimann, M., Esser, G., Haxeltine, A., Kaduk, J., Kicklighter, D. W., Knorr, W., Kohlmaier, G. H., Mcguire, A. D., Melillo, J., Iii, B. M., Ottofi, R. D., Prentice, I. C., Sauf, W., Schloss, A., Sitch, S., Wittenberg, U., and Wtirth, G.: Evaluation of terrestrial carbon cycle models through simulations of the seasonal cycle of atmospheric CO2: First results of a model intercomparison study, Global Biogeochemical Cycles, 12, 1–24, https://doi.org/10.1029/97GB01936, 1998.

Huo, D., Huang, X., Dou, X., Ciais, P., Li, Y., Deng, Z., Wang, Y., Cui, D., Benkhelifa, F., Sun, T., Zhu, B., Roest, G., Gurney, K. R., Ke, P., Guo, R., Lu, C., Lin, X., Lovell, A., Appleby, K., DeCola, P. L., Davis, S. J., and Liu, Z.: Carbon Monitor Cities near-real-time daily estimates of CO2 emissions from 1500 cities worldwide, Scientific Data, 9, 533, https://doi.org/10.1038/s41597-022-01657-z, 2022.

Huth, R., Beck, C., Philipp, A., Demuzere, M., Ustrnul, Z., Cahynová, M., Kyselý, J., and Tveito, O. E.: Classifications of atmospheric circulation patterns: Recent advances and applications, Annals of the New York Academy of Sciences, 1146, 105–152, https://doi.org/10.1196/annals.1446.019, 2008.

Kiel, M., Eldering, A., Roten, D. D., Lin, J. C., Feng, S., Lei, R., Lauvaux, T., Oda, T., Roehl, C. M., Blavier, J. F., and Iraci, L. T.: Urban-focused satellite CO2 observations from the Orbiting Carbon Observatory-3: A first look at the Los Angeles megacity, Remote Sensing of Environment, 258, 112 314, https://doi.org/10.1016/J.RSE.2021.112314, 2021.

Kort, E. A., Frankenberg, C., Miller, C. E., and Oda, T.: Space-based observations of megacity carbon dioxide, Geophysical Research Letters, 39, L17 806, https://doi.org/10.1029/2012GL052738, 2012.

Labzovskii, L. D., Jeong, S. J., and Parazoo, N. C.: Working towards confident spaceborne monitoring of carbon emissions from cities using Orbiting Carbon Observatory-2, Remote Sensing of Environment, 233, 111 359, https://doi.org/10.1016/j.rse.2019.111359, 2019.

Lei, R., Feng, S., Danjou, A., Broquet, G., Wu, D., Lin, J. C., O'dell, C. W., and Lauvaux, T.: Fossil fuel CO2 emissions over metropolitan areas from space: A multi-model analysis of OCO-2 data over Lahore, Pakistan, Remote Sensing of Environment, 264, 112 625, https://doi.org/10.1016/j.rse.2021.112625, 2021.

Lei, R., Feng, S., Xu, Y., Tran, S., Ramonet, M., Grutter, M., Garcia, A., Campos-Pineda, M., Lauvaux, T., Tropomi, S., Washington, W.-C., and Baltimore, D. C.: Reconciliation of asynchronous satellite-based NO2 and XCO2 enhancements with mesoscale modeling over two urban landscapes, Remote Sensing of Environment, 281, 113 241, https://doi.org/10.1016/j.rse.2022.113241, 2022.

Lindenmaier, R., Dubey, M. K., Henderson, B. G., Butterfield, Z. T., Herman, J. R., Rahn, T., and Lee, S. H.: Multiscale observations of CO2, 13CO2, and pollutants at Four Corners for emission verification and attribution, Proceedings of the National Academy of Sciences of the United States of America, 111, 8386–8391, https://doi.org/10.1073/PNAS.1321883111/-/DCSUPPLEMENTAL/PNAS.201321883SI.PDF, 2014.

Masarie, K. A. and Tans, P. P.: Extension and integration of atmospheric carbon dioxide data into a globally consistent measurement record, Journal of Geophysical Research, 100, 11,593–11,610, https://doi.org/10.1029/95jd00859, 1995.

McKain, K., Wofsy, S. C., Nehrkorn, T., Eluszkiewicz, J., Ehleringer, J. R., and Stephens, B. B.: Assessment of ground-based atmospheric observations for verification of greenhouse gas emissions from an urban region, Proceedings of the National Academy of Sciences, 109, 8423–8428, https://doi.org/10.1073/PNAS.1116645109/-/DCSUPPLEMENTAL/PNAS.1116645109_SI.PDF, 2012.

Miller, J. B., Lehman, S. J., Verhulst, K. R., Miller, C. E., Duren, R. M., Yadav, V., Newman, S., and Sloop, C. D.: Large and seasonally varying biospheric CO2 fluxes in the Los Angeles megacity revealed by atmospheric radiocarbon, Proceedings of the National Academy of Sciences of the United States of America, 117, 26 681–26 687, https://doi.org/10.1073/PNAS.2005253117/-/DCSUPPLEMENTAL, 2020.

https://doi.org/10.5194/essd-2025-234
Preprint. Discussion started: 17 June 2025

Mitchell, L. E., Lin, J. C., Bowling, D. R., Pataki, D. E., Strong, C., Schauer, A. J., Bares, R., Bush, S. E., Stephens, B. B., Mendoza, D., Mallia, D., Holland, L., Gurney, K. R., and Ehleringer, J. R.: Long-term urban carbon dioxide observations reveal spatial and temporal dynamics related to urban characteristics and growth, Proceedings of the National Academy of Sciences of the United States of America, 115, 2912–2917, https://doi.org/10.1073/PNAS.1702393115/-/DCSUPPLEMENTAL, 2018.

Monte-carlo, T. and Sun, T.: Increased concentration and vertical distribution of carbon dioxide in the stratosphere, Nature, 316, 708–710, 1985.

Nisbet, E. and Weiss, R.: Top-Down Versus Bottom-Up, Science, 328, 1241–1243, 2010.

Pan, G., Xu, Y., and Ma, J.: The potential of CO2 satellite monitoring for climate governance: A review, Journal of Environmental Management, 277, 111 423, https://doi.org/10.1016/j.jenvman.2020.111423, 2021.

Park, H., Jeong, S., Park, H., Labzovskii, L. D., and Bowman, K. W.: An assessment of emission characteristics of Northern Hemisphere cities using spaceborne observations of CO2, CO, and NO2, Remote Sensing of Environment, 254, 112 246, https://doi.org/10.1016/j.rse.2020.112246, 2021.

Piao, S., Ciais, P., Friedlingstein, P., Peylin, P., Reichstein, M., Luyssaert, S., Margolis, H., Fang, J., Barr, A., and Chen, A.: Net carbon dioxide losses of northern ecosystems in response to autumn warming, Nature, 451, 49–52, https://doi.org/10.1038/nature06444ï, 2008.

Reuter, M., Buchwitz, M., Hilboll, A., Richter, A., Schneising, O., Hilker, M., Heymann, J., Bovensmann, H., and Burrows, J. P.: Decreasing emissions of NOx relative to CO2 in East Asia inferred from satellite observations, Nature Geoscience, 7, 792–795, https://doi.org/10.1038/NGEO2257, 2014.

Reuter, M., Buchwitz, M., Schneising, O., Krautwurst, S., O'dell, C. W., Richter, A., Bovensmann, H., and Burrows, J. P.: Towards monitoring localized CO2 emissions from space: co-located regional CO2 and NO2 enhancements observed by the OCO-2 and S5P satellites, Atmos. Chem. Phys, 19, 9371–9383, https://doi.org/10.5194/acp-19-9371-2019, 2019.

Richter, A., Burrows, J. P., Nüß, H., Granier, C., and Niemeier, U.: Increase in tropospheric nitrogen dioxide over China observed from space, Nature, 437, 129–132, https://doi.org/10.1038/nature04092, 2005.

Schneising, O., Heymann, J., Buchwitz, M., Reuter, M., Bovensmann, H., and Burrows, J. P.: Anthropogenic carbon dioxide source areas observed from space: assessment of regional enhancements and trends, Atmos. Chem. Phys, 13, 2445–2454, https://doi.org/10.5194/acp-13-2445-2013, 2013.

Schwandner, F. M., Gunson, M. R., Miller, C. E., Carn, S. A., Eldering, A., Krings, T., Verhulst, K. R., Schimel, D. S., Nguyen, H. M., Crisp, D., O'dell, C. W., Osterman, G. B., Iraci, L. T., and Podolske, J. R.: Spaceborne detection of localized carbon dioxide sources, science, 358, eaam5782, https://doi.org/10.1126/science.aam5782, 2017.

Shen, M., Tang, Y., Chen, J., Yang, X., Wang, C., Cui, X., Yang, Y., Han, L., Li, L., Du, J., Zhang, G., and Cong, N.: Earlier-Season Vegetation Has Greater Temperature Sensitivity of Spring Phenology in Northern Hemisphere, PLOS ONE, 9, e88 178, https://doi.org/10.1371/JOURNAL.PONE.0088178, 2014.

Shim, C., Lee, J., and Wang, Y.: Effect of continental sources and sinks on the seasonal and latitudinal gradient of atmospheric carbon dioxide over East Asia, Atmospheric Environment, 79, 853–860, https://doi.org/10.1016/J.ATMOSENV.2013.07.055, 2013.

Streets, D. G., Canty, T., Carmichael, G. R., De Foy, B., Dickerson, R. R., Duncan, B. N., Edwards, D. P., Haynes, J. A., Henze, D. K., Houyoux, M. R., Jacob, D. J., Krotkov, N. A., Lamsal, L. N., Liu, Y., Lu, Z., Martin, R. V., Pfister, G. G., Pinder, R. W., Salawitch, R. J., and Wecht, K. J.: Emissions estimation from satellite retrievals: A review of current capability, Atmospheric Environment, 77, 1011–1042, https://doi.org/10.1016/j.atmosenv.2013.05.051, 2013.

https://doi.org/10.5194/essd-2025-234
Preprint. Discussion started: 17 June 2025

Tang, R., He, B., Chen, H. W., Chen, D., Chen, Y., Fu, Y. H., Yuan, W., Li, B., Li, Z., Guo, L., Hao, X., Sun, L., Liu, H., Sun, C., and Yang, Y.: Increasing terrestrial ecosystem carbon release in response to autumn cooling and warming, Nature Climate Change, 12, 380–385, https://doi.org/10.1038/s41558-022-01304-w, 2022.

Tans, P. P., Conway, T. J., and Nakazawa, T.: Latitudinal distribution of the sources and sinks of atmospheric carbon dioxide derived from surface observations and an atmospheric transport model, Journal of Geophysical Research, 94, 5151–5172, https://doi.org/10.1029/JD094iD04p05151, 1989.

Taylor, J. A. and Orr, J. C.: The natural latitudinal distribution of atmospheric CO2, Global and Planetary Change, 26, 375–386, https://doi.org/10.1016/S0921-8181(00)00050-3, 2000.

Van Der Werf, G. R., Randerson, J. T., Giglio, L., Van Leeuwen, T. T., Chen, Y., Rogers, B. M., Mu, M., Van Marle, M. J., Morton, D. C., Collatz, G. J., Yokelson, R. J., and Kasibhatla, P. S.: Global fire emissions estimates during 1997-2016, Earth System Science Data, 9, 697–720, https://doi.org/10.5194/essd-9-697-2017, 2017.

Verhulst, K. R., Karion, A., Kim, J., Salameh, P. K., Keeling, R. F., Newman, S., Miller, J., Sloop, C., Pongetti, T., Rao, P., Wong, C., Hopkins, F. M., Yadav, V., Weiss, R. F., Duren, R. M., and Miller, C. E.: Carbon dioxide and methane measurements from the Los Angeles Megacity Carbon Project - Part 1: Calibration, urban enhancements, and uncertainty estimates, Atmospheric Chemistry and Physics, 17, 8313–8341, https://doi.org/10.5194/acp-17-8313-2017, 2017.

Wang, R., Xiong, Y., Xing, X., Yang, R., Li, J., Wang, Y., Cao, J., Balkanski, Y., Peñuelas, J., Ciais, P., Hauglustaine, D., Sardans, J., Chen, J., Ma, J., Xu, T., Kan, H., Zhang, Y., Oda, T., Morawska, L., Zhang, R., and Tao, S.: Daily CO2 Emission Reduction Indicates the Control of Activities to Contain COVID-19 in China, The Innovation, 1, https://doi.org/10.1016/j.xinn.2020.100062, 2020.

Wu, C., Yang, S., Jiao, D., Chen, Y., Yang, J., and Huang, B.: Estimation of daily XCO2 at 1 km resolution in China using a spatiotemporal ResNet model, Science of The Total Environment, 954, 176 171, https://doi.org/10.1016/j.scitotenv.2024.176171, 2024.

Wu, D., Lin, J. C., Oda, T., and Kort, E. A.: Space-based quantification of per capita CO2 emissions from cities, Environmental Research Letters, 15, 035 004, https://doi.org/10.1088/1748-9326/AB68EB, 2020.

Ye, X., Lauvaux, T., Kort, E. A., Oda, T., Feng, S., Lin, J. C., Yang, E. G., and Wu, D.: Constraining Fossil Fuel CO2 Emissions From Urban Area Using OCO-2 Observations of Total Column CO2, Journal of Geophysical Research: Atmospheres, 125, 1–29, https://doi.org/10.1029/2019JD030528, 2020.

Yun, J., Jeong, S., Gruber, N., Gregor, L., Ho, C. H., Piao, S., Ciais, P., Schimel, D., and Kwon, E. Y.: Enhance seasonal amplitude of atmospheric CO2 by the changing Southern Ocean carbon sink, Science Advances, 8, https://doi.org/10.1126/SCIADV.ABQ0220, 2022.

Zanaga, D., Van De Kerchove, R., Daems, D., De Keersmaecker, W., Brockmann, C., Kirches, G., Wevers, J., Cartus, O., Santoro, M., Fritz, S., Lesiv, M., Herold, M., Tsendbazar, N.-E., Xu, P., Ramoino, F., and Arino, O.: ESA WorldCover 10 m 2021 v200, https://doi.org/10.5281/zenodo.7254221, 2022.

Zeng, N., Han, P., Liu, Z., Liu, D., Oda, T., Martin, C., Liu, Z., Yao, B., Sun, W., Wang, P., Cai, Q., Dickerson, R., and Maksyutov, S.: Global to local impacts on atmospheric CO2 from the COVID-19 lockdown, biosphere and weather variabilities, Environmental Research Letters, 17, 015 003, https://doi.org/10.1088/1748-9326/ac3f62, 2021.

Zhao, M., Cheng, C., Zhou, Y., Li, X., Shen, S., and Song, C.: A global dataset of annual urban extents (1992-2020) from harmonized nighttime lights, Earth Syst. Sci. Data, 14, 517–534, https://doi.org/10.5194/essd-14-517-2022, 2022.

Zhou, Y., Fan, P., Liu, J., Xu, Y., Huang, B., and Webster, C.: GloCE v1.0: Global CO2 Enhancement Dataset 2019-2023 [Data set]. Zenodo., https://doi.org/10.5281/zenodo.15209825, 2025.